14th International Symposium on Turbulence and Shear Flow Phenomena (TSFP14)
Heidelberg, Germany, July 28–31, 2026

CORRELATION OF ENERGY EXTRACTION EFFICIENCY OF AN AUTOROTATING FLAT PLATE WITH NEAR-WAKE VORTICAL STRUCTURES

Bhramar Pustode
Department of Applied Mechanics
Indian Institute of Technology Delhi
New Delhi, 110016, India
amz228604@iitd.ac.in

Narsing Kumar Jha
Department of Applied Mechanics
Indian Institute of Technology Delhi
New Delhi, 110016, India
narsingjha@am.iitd.ac.in

Amitabh Bhattacharya
Department of Applied Mechanics
Indian Institute of Technology Delhi
New Delhi, 110016, India
bhattach@am.iitd.ac.in

ABSTRACT

This study investigates a simplified drag-based vertical-axis wind turbine consisting of an autorotating rectangular flat plate. The plate is mounted about its mid-chord and subjected to cross-flow to exploit wind-induced autorotation for energy harvesting. A custom-built non-contact eddy-current damper is used as a proxy for a generator load. Time-resolved particle image velocimetry (2D-2C TR-PIV) measurements are performed in the near-wake region to examine the relationship between vortex dynamics and the power coefficient over a range of tip-speed ratios. The temporal evolution of the retreating-edge vortex (REV) and advancing-edge vortices (AEVs) is quantified in terms of circulation, vortical area, and duty cycle for representative cases at $\lambda = 0.32, 0.29$, and 0.22 at constant generator loading. Ratios of these quantities between REV (energy-producing structures) and AEVs (energy-dissipating structures) are defined to characterize their relative contributions and are correlated with the power coefficient. The highest-performance case ($\lambda = 0.32, C_p = 7.6\%$) exhibits approximately 35% higher circulation and area-based ratios, along with about 20% higher temporal persistence, compared to the lowest-performance case ($\lambda = 0.22, C_p = 3.4\%$). Spectral analysis further shows that the dominant vortex shedding frequency aligns with the blade passing frequency, indicating strong synchronization between vortex dynamics and plate motion. Higher C_p cases exhibit greater spectral energy concentration in the primary peak, reflecting more coherent vortex shedding. Overall, the results establish a clear link between vortex coherence, spectral characteristics, and energy extraction efficiency in an autorotating flat plate.

1 INTRODUCTION

Drag-based vertical-axis turbines have been extensively studied using experiments and CFD simulations (Akwa *et al.* (2012)). Most prior work has focused on evaluating energy extraction efficiency under varying flow conditions and characterizing the associated flow structures (Fernando *et al.* (2020)). However, the specific role of unsteady flow dynamics in governing energy generation remains largely unexplored for systems such as autorotating flat plates. Specifically, a clear mechanistic understanding of how vortical structures, particularly the retreating-edge vortex (REV) and advancing-edge vortices (AEVs), interact with the plate to generate torque remains limited (Menon & Mittal (2021)). Furthermore, the connection between phase-resolved vortex dynamics and their spectral characteristics in the frequency domain remains largely unexplored.

Autorotation of bluff bodies in cross-flow is characterized by strongly coupled fluid-structure interactions, wherein the rotating body and the surrounding flow evolve simultaneously and influence each other (Lugt (1980)). The dynamics of the autorotating system are governed by non-dimensional parameters such as Reynolds number, torsional damping coefficient (generator load), and polar moment of inertia for a fixed aspect and thickness ratio of a flat plate.

In the present study, wind tunnel experiments are conducted over a range of operating parameters, including Reynolds number, generator load, and polar mass moment of inertia, to characterize autorotation response. The focus of the current work is twofold. (a) First, the phase-averaged near-wake flow field is analyzed to characterize the evolution of REV and AEV structures. Their circulation, vortical area, and temporal persistence are quantified, and the resulting vortex-based metrics are correlated with the power coefficient to identify the key mechanisms governing energy extraction. (b) Second, frequency-domain analysis using FFT is performed to examine dominant flow frequencies and spectral energy distribution, establishing a link between vortex dynamics, spectral coherence, and energy extraction efficiency.

2 Experimental methodology

2.1 Flow facility and flat-plate model

Experiments were conducted in a suction-type, open-circuit, subsonic wind tunnel with a test section of $5\,\mathrm{m} \times$

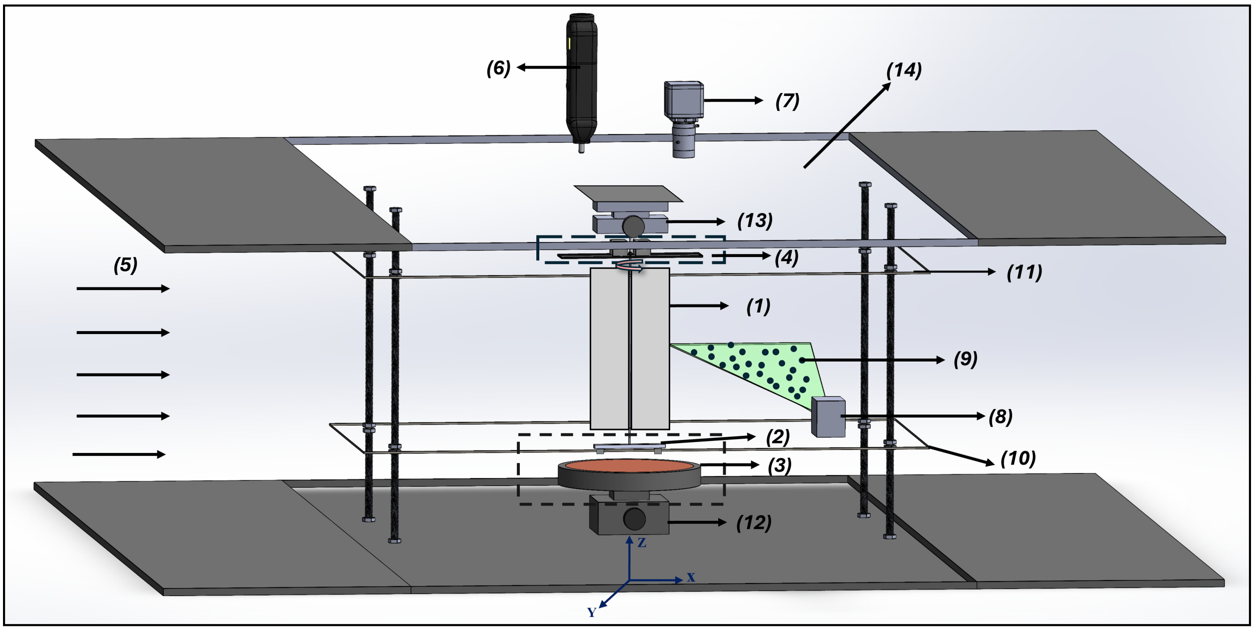

Figure 1. (Colour online) (a) Schematic of the experimental setup used to study autorotation of a flat plate in the wind tunnel. The figure annotations identify the following components/systems: (1) flat plate mounted on a shaft, (2) neodymium magnets (eddy-current damper component), (3) copper plate (eddy-current damper component), (4) additional mass moment of inertia assembly, (5) free-stream velocity direction, (6) digital non-contact tachometer, (7) high-speed camera, (8) continuous wave laser, (9) laser sheet and tracer particles, (10) lower end plate, (11) upper end plate, (12) micro-drive stage for maintaining the gap between magnets and the copper plate, (13) XY stage for alignment of the overall assembly, and (14) transparent optical sheet for imaging.

$0.75\,\mathrm{m} \times 0.5\,\mathrm{m}$ (length $\times$ width $\times$ height). The tunnel provided a free-stream velocity range of $0.5\,\mathrm{m/s}$ to $17.2\,\mathrm{m/s}$, with a low turbulence intensity of 1%.

A rectangular flat plate made of poly-methyl methacrylate (PMMA, acrylic), with a length-to-chord aspect ratio ($AR = 2$) and thickness-to-chord ratio ($\tau = 0.023$), was used. The plate was mounted on a stainless steel shaft (SS316) passing through its mid-chord and supported at both ends by low-friction bearings (make: SKF), as illustrated in annotation (1) of Figure 1. The shaft alignment was carefully adjusted and verified to within 1° using a self-leveling cross-line laser (Class II). End plates were installed at both ends of the assembly to enforce two-dimensionality in the mean flow. The maximum area blockage induced by the flat plate was approximately 7%, and therefore, no blockage correction was applied to the measured autorotation rate (Miller *et al.* (2018)). Autorotation was initiated by imparting a small angular perturbation to overcome the static equilibrium of the mid-chord mounted plate.

The governing non-dimensional parameters for the present study are the Reynolds number Re, torsional damping coefficient C_g^*, polar mass moment of inertia I^*, and the tip-speed ratio λ, defined as

$$Re = \frac{U_\infty c}{\nu}; \quad C_g^* = \frac{C_g}{\rho_a c^3 l U_\infty}; \quad I^* = \frac{I_s + I_a}{\rho_a c^4 l}; \quad \lambda = \frac{c\,\overline{\dot{\theta}}}{2U_\infty} \tag{1}$$

Here, U_∞ is the free-stream velocity, c is the chord length, ν is the kinematic viscosity of air, ρ_a is the air density, l is the span, C_g is the torsional damping coefficient, I_s is the structural mass moment of inertia, I_a is the added polar mass moment of inertia due to the surrounding fluid, and $\overline{\dot{\theta}}$ is the mean autorotation rate, averaged over at least 30 cycles. The mean autorotation rate was measured using a non-contact digital tachometer (Kusam-MECO, model KM-2241) with a resolution of 0.1 RPM. The polar mass moment of inertia I^* was varied from 4 to 15 by placing additional masses at different radial locations from the axis of rotation, as illustrated in annotation (4) of Figure 1. All experiments were conducted at a laboratory temperature of 24 ± 2°C under standard atmospheric conditions.

2.2 Power extraction mechanism

Energy extraction was achieved using a custom-built eddy-current-based torsional damper comprising a stationary copper plate and rotating neodymium magnets (Figure 1, annotations (2) and (3)). This configuration mimics a generator load with a controllable torsional damping coefficient C_g. The damping is tuned by varying the gap G between rotating magnets and a stationary copper plate, similar to Soti *et al.* (2018). The extracted power is given by $P_e = C_g\,\overline{\dot{\theta}^2}$. The power coefficient is thus defined as the ratio of extracted power to the available fluid power and is given as follows:

$$C_p = \frac{P_e}{P_f} = \frac{2C_g\,\overline{\dot{\theta}^2}}{\rho_a A_p U_\infty^3} \times 100\% \tag{2}$$

where $A_p = c\,l$ is the projected area of the plate.

2.3 Flow diagnostics

Velocity and vorticity fields in the near-wake region were obtained using planar time-resolved particle image velocimetry. The flow was seeded with ethylene glycol fog particles having a nominal diameter of 1-3 μm, introduced using a fog generator (make: Stan Z-1500). Seeding was injected approximately 10 m upstream of the test section, ahead of the tunnel impeller, to ensure uniform particle distribution and adequate mixing. The seeded flow was illuminated using a 5 W

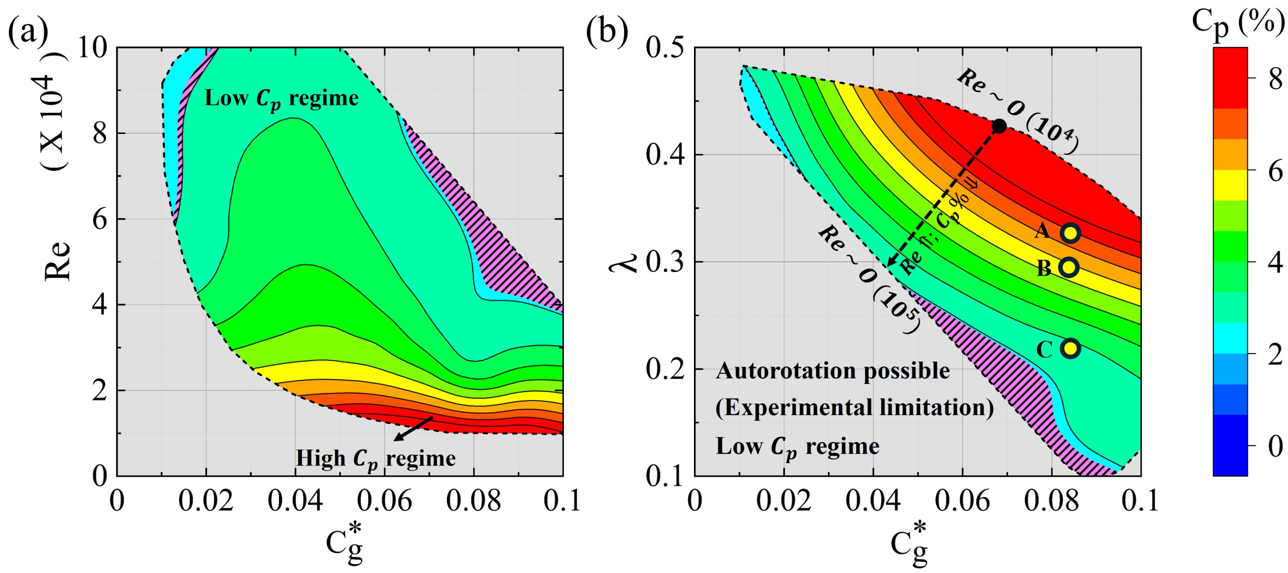

Figure 2. (Colour online) Contours of the power coefficient in the non-dimensional domain: (a) Reynolds number versus torsional damping coefficient; (b) tip-speed ratio versus torsional damping coefficient. Red regions indicate higher power coefficients, and blue regions indicate lower power coefficients. The yellow markers (A–C) in panel (b) indicate cases at constant torsional damping $C_g^* = 0.082$ with varying tip-speed ratios, selected for further analysis.

continuous-wave Nd:YAG laser ($\lambda = 532$ nm, make: CNI) equipped with a cylindrical concave lens to generate a thin laser sheet of approximately 2 mm. Image acquisition was carried out using a Photron Fast-Cam Mini UX-100 fitted with a 25 mm $f/2.8$ lens. Image sequences were recorded at a frame rate of 1000 Hz with a shutter speed of $1/2000$ s and a resolution of 1280×1080 pixels. Each experiment was recorded for 8.7 s (8700 snapshots), capturing at least 30 half-rotation cycles ($0^\circ \leq \theta \leq 180^\circ$). The acquired images were processed using the PIVlab suite on MATLAB (version 3.06) (Stamhuis & Thielicke (2014)), employing a multi-pass FFT window deformation algorithm with four successive passes of decreasing interrogation window size. The final interrogation window size was 64×64 pixels with 50% overlap, resulting in a spatial resolution of $\Delta x = 0.054c$. The spanwise vorticity field, $\omega_z = \partial v/\partial x - \partial u/\partial y$, was phase-averaged at azimuthal positions $\theta = 2^\circ \pm 0.3^\circ$ over the range $0^\circ \leq \theta \leq 180^\circ$, using data from a minimum of 30 half-cycles. A nearly constant angular velocity was assumed for phase binning.

Vortex structures were identified using the Q-criterion. A threshold of $Q > 0.1\,Q_{\max}$ was applied, where $Q_{\max}$ is defined as the mean of the ten highest Q values in the flow field to isolate coherent vortical structures from background noise (Menon & Mittal (2021)). The spanwise circulation was computed at every 2° interval using Stokes' theorem within the identified vortex boundaries as $\Gamma = \int \omega_z \, dA$ where $dA = dx\,dy$ is the differential area element. The vortical area is defined as $A = n\,\mathrm{d}x\,\mathrm{d}y$, where n is the number of grid points satisfying $Q > 0.1\,Q_{\max}$, and $\mathrm{d}x\,\mathrm{d}y$ is the area of an individual grid cell.

3 Results

The results are organized into four sections. Section 3.1 presents the power coefficient contour maps at varying levels of torsional damping coefficients, Reynolds numbers, and tip-speed ratios. Sections 3.2-3.4 focus on three representative cases (labelled A, B, and C in Figure 2(b)) at constant $C_g^* = 0.082$ with $\lambda = 0.32$, 0.29, and 0.22 with associated power coefficients of 7.6%, 6.7%, and 3.4%. Section 3.2 examines phase-averaged flow fields, focusing on the formation and evolution of the retreating-edge vortex (REV) and advancing-edge vortices (AEVs) over the rotation cycle. Section 3.3 analyses the circulation and vortical area of REV and AEV and their correlation with the power coefficient, while Section 3.4 investigates velocity spectra to identify dominant flow frequencies and energetics of the flow structures.

3.1 Power coefficient contours

Experiments were conducted by systematically varying the Reynolds number Re, torsional damping coefficient C_g^*, and polar mass moment of inertia I^*. The Reynolds number was varied via the free-stream velocity, the damping coefficient was controlled by adjusting the gap in the eddy-current damper, and the inertia was varied by changing the radial location of additional masses.

Using dimensional analysis, the tip-speed ratio and power coefficient for an autorotating flat plate (at fixed AR and τ) can be expressed as $\lambda = f_1(Re, C_g^*, I^*)$ and $C_p = f_2(Re, C_g^*, I^*)$. Figure 2 presents the contour maps of C_p in the parameter space of Re, C_g^*, and λ. The ranges explored are $Re \in [0.5 \times 10^3, 1 \times 10^5]$, $C_g^* \in [0.01, 0.10]$, $I^* \in [4, 15]$, and $\lambda \in [0.05, 0.50]$, within which C_p varies between 0.5% and 8%. The dataset comprises approximately 300 experiments (each with three realizations), each corresponding to a unique combination of Re, C_g^*, I^*, and λ. The repeated measurements show good consistency, with variations in C_p remaining within ±5%. An optimal operational regime is identified at low Reynolds numbers $Re \in [1 \times 10^4, 4 \times 10^4]$, moderate torsional damping $C_g^* \in [0.04, 0.10]$, and intermediate tip-speed ratios $\lambda \in [0.25, 0.45]$, where C_p attains values between 4% and 8%. This region is referred to as the *optimal autorotation zone* (or *sweet spot*), representing the most efficient operating conditions for power extraction. Beyond $I^* > 10$, no significant variation in C_p is observed, indicating that the results are largely independent of the moment of inertia.

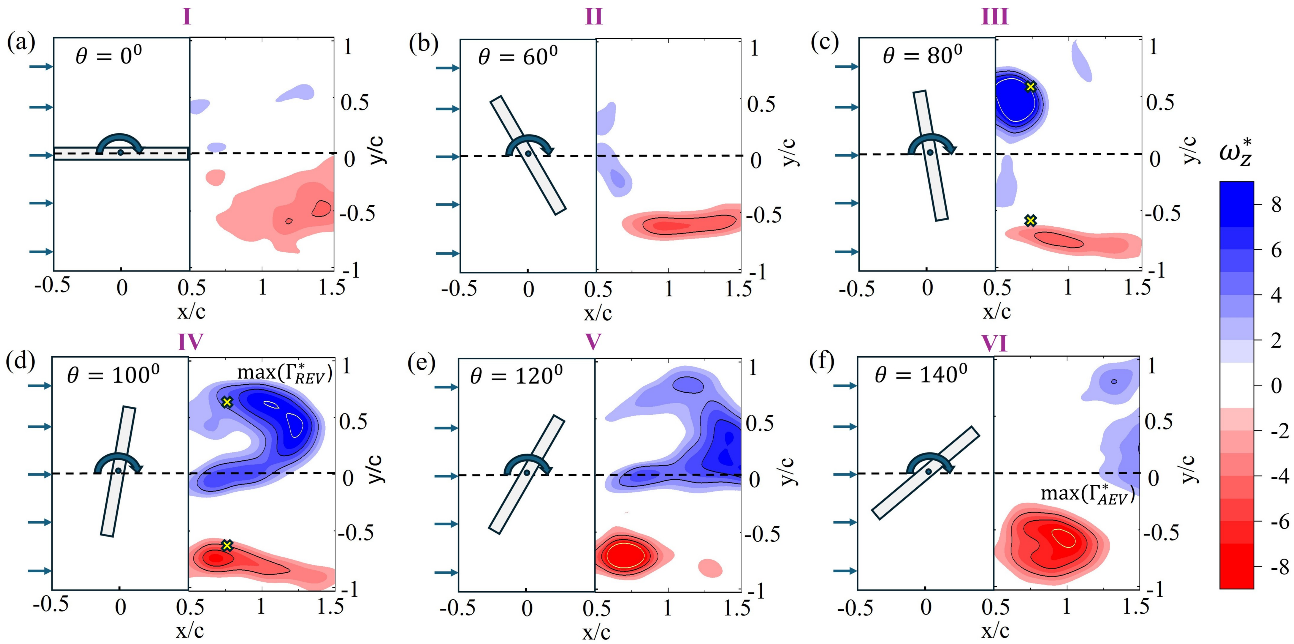

Figure 3. (Colour online) Phase-averaged spanwise vorticity ω_z^* in the near-wake region for a representative case A with $\lambda = 0.32$: (a) $\theta = 0°$, (b) $\theta = 60°$, (c) $\theta = 80°$, (d) $\theta = 100°$, (e) $\theta = 120°$, and (f) $\theta = 140°$. Blue and red contours denote the retreating-edge vortex (REV) and advancing-edge vortices (AEVs), respectively. The dark yellow contour line indicates regions of strong vorticity, defined by $\omega_z^* > 8$. Measurements were performed in the streamwise mid-span plane over a fixed field of view: $x/c \in [0.5, 1.5]$ and $y/c \in [-1, 1]$, where x and y denote the streamwise and transverse directions. The plate center is at $(0,0)$, with clockwise rotation and freestream from left to right. Both spatial coordinates are normalized by the chord length c.

3.2 Phase-averaged flow fields and vorticity dynamics

To understand the flow physics underlying the variation in power coefficient, time-resolved PIV measurements were performed across a range of operating conditions. Figure 3 shows the phase-averaged, non-dimensional spanwise vorticity field for the representative high-performance case A ($\lambda = 0.32$), where $\omega_z^* = \omega_z c/U_\infty$. The flow field reveals the formation, growth, and shedding of vortical structures over the rotation cycle. During each half-revolution, multiple vortices are generated, including both isolated structures and elongated vortex trails. A consistent shedding pattern is observed: a single large, coherent vortex forms on the retreating edge, while weaker, sheet-like vortices are shed from the advancing edge. The vortex, rotating in the same direction as the plate, is identified as the retreating-edge vortex (REV), whereas the counter-rotating sheet-like structures, are referred to as advancing-edge vortices (AEVs), similar to Uchibori & Tamura (2019) . As the REV convects downstream, it deforms and eventually undergoes bursting at approximately $x/c \approx 0.7$-0.9. Although the exact mechanism of this breakdown remains unclear, it is likely associated with three-dimensional vortex interactions and the inherent instability of large-scale vortical structures (Medina & Jones (2016)).

The REV exhibits a characteristic horseshoe-shaped three-dimensional structure, commonly associated with rotating bluff bodies, as shown in Figure 3(d); similar structures have been reported by Rolin & Porté-Agel (2018). In contrast, the AEVs appear as persistent sheet-like trailing vortices present throughout the rotation cycle, followed by relatively weaker coherent vortices, particularly at later phases $\theta \approx 140°$-$160°$ (Figure 3(f)). The relative strength, temporal persistence, and coherence of the REV compared to the AEVs are therefore expected to play a key role in determining the overall energy extraction.

3.3 Phase-resolved evolution of circulation and vortical area

Using the Q-criterion, vortical structures were identified, and the circulation strength and vortical area of the retreating-edge vortex (REV) and advancing-edge vortices (AEVs) were quantified. The non-dimensional circulation is defined as $\Gamma^*_{\mathrm{REV}} = \Gamma_{\mathrm{REV}}/(cU_\infty)$ and $\Gamma^*_{\mathrm{AEV}} = \Gamma_{\mathrm{AEV}}/(cU_\infty)$. and are presented as a function of azimuthal angle in Figure 4(a-b).

The REV circulation shows a single dominant peak over each half-revolution, corresponding to the formation and shedding of a primary coherent vortex (Figure 4(a)). The peak occurs at $\theta \approx 90°$–$120°$, with a maximum value of approximately 2.2 for $\lambda = 0.32$. As λ decreases, the peak circulation reduces, indicating a weakening of the primary energy-producing vortex. In contrast, the AEV circulation exhibits a more complex structure, with a primary peak at $\theta \approx 120°$–$150°$ and secondary peaks distributed over $\theta \approx 0°$–$90°$ (Figure 4(b)), reflecting more fragmented and less coherent vortex dynamics.

Based on the above observations, a set of non-dimensional parameters is introduced to quantify the relative strength of the REV and AEV structures within the field of view. The peak circulation strength ratio γ and vortical area ratio Λ of REV with respect to AEVs are defined as:

$$\gamma = \frac{\mathrm{peak}(\Gamma^*_{\mathrm{REV}})}{\sum_{i=1}^{N} \mathrm{peak}(\Gamma^*_{\mathrm{AEV}_i})}; \quad \Lambda = \frac{\mathrm{peak}(A^*_{\mathrm{REV}})}{\sum_{i=1}^{N} \mathrm{peak}(A^*_{\mathrm{AEV}_i})} \tag{3}$$

where $A^*_{\mathrm{AEV}_i}$ represent the areas of the i^{th} AEV vortices within

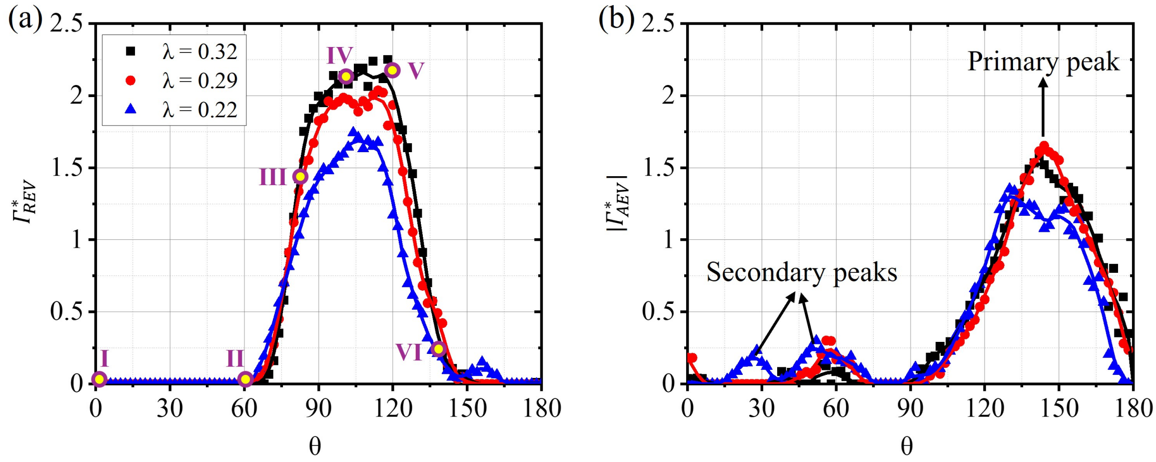

Figure 4. (Colour online) Circulation of the retreating-edge vortex (REV) and advancing-edge vortex (AEV) at varying tip-speed ratios. (a) Non-dimensional REV circulation versus azimuthal angle, (b) non-dimensional AEV circulation versus azimuthal angle. The labelled positions (I-VI) for the $\lambda = 0.32$ case correspond to the phase-averaged flow fields shown in Figure 3. Solid lines represent five-point weighted moving averages. Vortex identification is based on a threshold of $Q > 0.1\,Q_{\max}$ for all cases.

Table 1. Ratio of peak circulation and vortical area of REV with respect to AEV at varying λ and C_p.

Case	λ	C_p (%)	γ	Λ
A	0.32	7.6	1.34	1.24
B	0.29	6.7	1.04	1.19
C	0.22	3.4	0.85	0.83

a half rotation cycle. The number of AEV peaks is taken as $N = 2$ for $\lambda = 0.32$ and 0.29, and $N = 3$ for $\lambda = 0.22$, based on the observed circulation profiles.

The results presented in Table 1 show a clear correlation between the vortex-based metrics and the power coefficient. Case A ($\lambda = 0.32$, $C_p = 7.6\%$) exhibits higher peak circulation ratios, larger vortical area ratios, and longer REV duty cycles relative to the AEVs. This indicates that efficient energy extraction is associated with a strong, coherent, and persistent REV that dominates over dissipative AEV structures.

3.4 Velocity spectra: Dominant flow frequencies and energy distribution

The spectral content of the transverse velocity fluctuations, $v'(t)$, was analyzed at representative locations in the REV, AEV, and centerline regions. Spectral analysis was performed using Welch's method (pwelch) on velocity signals containing approximately 10^4 samples (corresponding to a minimum of 30 half-cycles), ensuring statistical convergence. The resulting power spectral density (PSD) is plotted as a function of the Strouhal number $St_c = f_{vs}c/U_\infty$, where f_{vs} denotes the vortex shedding frequency, for $\lambda = 0.32$, 0.29, and 0.22 (Figures 5(a) and 5(b)). Figure 5(a) corresponds to a representative location in the REV region ($x/c = 0.75$, $y/c = 0.6$), while Figure 5(b) corresponds to a location in the AEV region ($x/c = 0.75$, $y/c = -0.6$), as indicated by the yellow markers in Figure 3(d).

The FFT spectra across different spatial locations and tip-speed ratios exhibit qualitatively similar features, characterized by a dominant peak followed by harmonics, an inertial subrange, and a dissipation regime. For all cases, the energy spectrum shows a clear first dominant peak corresponding to the vortex shedding frequency f_{vs}, where most of the spectral energy is concentrated. This dominant peak closely corresponds to the blade passing frequency (BPF), defined as $\text{BPF} = 2f_r$, where f_r is the rotational frequency of the flat plate. More precisely, f_{vs} lies within the range 0.90-1.15 BPF, indicating lock-in between vortex shedding and plate rotation.

A clear dependence on tip-speed ratio is observed in the spectral energy distribution. Case A with $\lambda = 0.32$ and $C_p = 7.6\%$ exhibits overall higher PSD magnitudes across the energy-containing range, consistent with stronger and more coherent vortex dynamics. In contrast, the lower tip-speed ratio case C with $\lambda = 0.22$ and $C_p = 3.4\%$ shows reduced PSD levels in the energy-containing range but relatively higher energy in the dissipation region. In the inertial range, the PSD in the REV region exhibits a shallower spectral decay ($\sim f^{-2}$), whereas the AEV region shows a steeper decay ($\sim f^{-3}$). This suggests that the REV region is more coherent and energetically efficient, whereas the AEV region is more dissipative.

The vortex shedding frequency and the corresponding Strouhal number were evaluated at 12 spectral locations (in REV, AEV, and centerline regions) for tip-speed ratios in the range $\lambda = 0.22$ to 0.38, and the results are presented in Figure 5(c). The mean and standard deviation of St_c were computed across these spatial locations, with the standard deviation found to be less than 10% of the mean, indicating strong spatial coherence and the dominance of a single frequency. The variation of St_c with λ is found to be approximately linear and can be expressed as $St_c \approx 2\lambda/\pi$, based on the relations $f_{vs} \approx \text{BPF} = 2f_r$, $St_c = f_{vs}c/U_\infty$, and $\lambda = c\pi f_r/U_\infty$. Optimal energy extraction occurs near $\lambda \approx 1/3$, corresponding to $St_c \approx 0.21$, where higher C_p values are observed.

The spectral energy percentage, E_1^*, is defined as the fraction of energy contained within the first dominant peak, bounded by the Strouhal number range $[a,b]$ in the neighborhood of the peak, such that $E_1^* = \left(\sum_{St_c=a}^{b} PSD\,\Delta St_c\right) \times \left(\sum_{St_c=0.1}^{\infty} PSD\,\Delta St_c\right)^{-1} \times 100\%$. The value of E_1^* is maximum at $\lambda \approx 1/3$, where approximately 55% of the spectral energy is contained within the first dominant peak in the AEV region and about 40% in the REV region (Figure 5(d)).

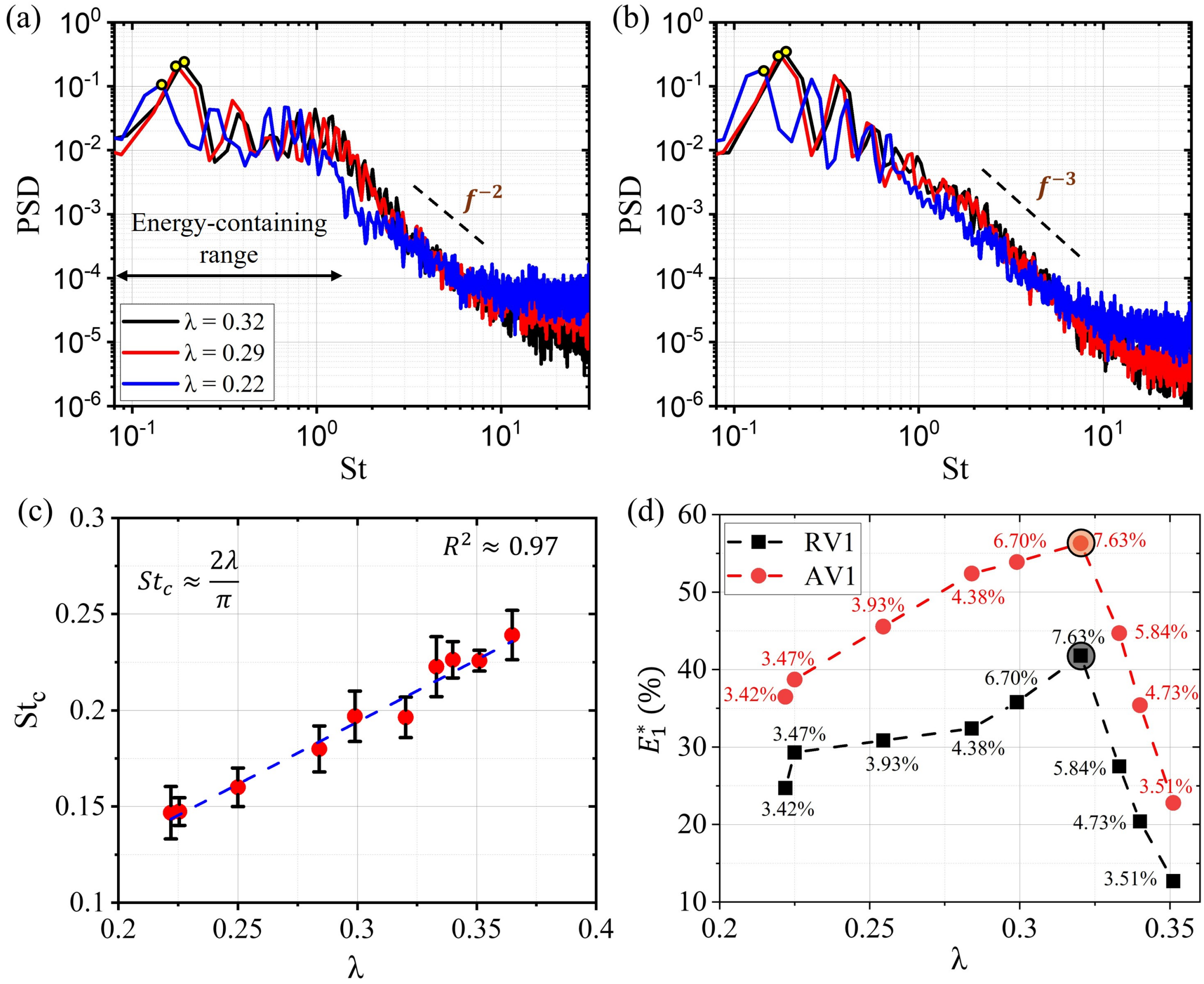

Figure 5. (Colour online) Normalized energy spectra (PSD) at tip-speed ratios $\lambda = 0.32, 0.29, 0.22$ for (a) a point in the REV region and (b) a point in the AEV region (see yellow markers in Figure 3(d) for spectral locations). (c)Variation of St_c with λ for 10 cases, showing linear dependence; error bars indicate standard deviation across 12 spectral locations. (d) Variation of the percentage of spectral energy in the first dominant peak with λ, with corresponding power coefficient values annotated at each data point.

4 Conclusions

This study examines the power coefficient of an autorotating flat plate over a range of Reynolds numbers, torsional damping coefficients, polar mass moment of inertia, and tip-speed ratios. An effort is made to correlate near-wake vortex dynamics with energy extraction. Overall, efficient energy extraction is associated with strong REV dominance, coherent vortex dynamics, and concentrated spectral energy. In contrast, increased spectral spreading and dissipation in AEV-dominated flows lead to reduced performance.

REFERENCES

Akwa, Joao Vicente, Vielmo, Horacio Antonio & Petry, Adriane Prisco 2012 A review on the performance of savonius wind turbines. *Renewable and sustainable energy reviews* **16** (5), 3054–3064.

Fernando, Porté-Agel, Majid, Bastankhah & Sina, Shamsoddin 2020 Wind-turbine and wind-farm flows: A review. *Boundary Layer Meteorology* **174** (1), 1–59.

Lugt, Hans J 1980 Autorotation of an elliptic cylinder about an axis perpendicular to the flow. *Journal of Fluid Mechanics* **99** (4), 817–840.

Medina, Albert & Jones, Anya R 2016 Leading-edge vortex burst on a low-aspect-ratio rotating flat plate. *Physical Review Fluids* **1** (4), 044501.

Menon, Karthik & Mittal, Rajat 2021 On the initiation and sustenance of flow-induced vibration of cylinders: insights from force partitioning. *Journal of Fluid Mechanics* **907**, A37.

Miller, Mark A, Duvvuri, Subrahmanyam, Brownstein, Ian, Lee, Marcus, Dabiri, John O & Hultmark, Marcus 2018 Vertical-axis wind turbine experiments at full dynamic similarity. *Journal of Fluid Mechanics* **844**, 707–720.

Rolin, Vincent FC & Porté-Agel, Fernando 2018 Experimental investigation of vertical-axis wind-turbine wakes in boundary layer flow. *Renewable energy* **118**, 1–13.

Soti, Atul Kumar, Zhao, Jisheng, Thompson, Mark C, Sheridan, John & Bhardwaj, Rajneesh 2018 Damping effects on vortex-induced vibration of a circular cylinder and implications for power extraction. *Journal of Fluids and Structures* **81**, 289–308.

Stamhuis, Eize & Thielicke, William 2014 Pivlab–towards user-friendly, affordable and accurate digital particle image velocimetry in matlab. *Journal of open research software* **2** (1), 30.

Uchibori, Kazuaki & Tamura, Tetsuro 2019 Les study on aerodynamics of auto-rotating square flat plate by ibm and samr. *Journal of Fluids and Structures* **89**, 108–122.